2D ANISOTROPIC COMPLEX-PADÉ HYBRID FINITE-DIFFERENCE DEPTH MIGRATION

D. Amazonas, R. Aleixo, J. Schleicher and J. Costa

email: *daniela.amazonas@gmail.com*

keywords: *Wave-equation migration, anisotropy, complex-Padé approximation*

ABSTRACT

Standard real-valued finite-difference (FD) and Fourier finite-difference (FFD) migrations cannot handle evanescent waves correctly, which can lead to numerical instabilities in the presence of strong velocity variations. A possible solution to these problems is the complex Padé approximation, which avoids problems with evanescent waves by a rotation of the branch cut of the complex square root. In this paper, we apply this approximation to the acoustic wave equation for vertical transversely anisotropic (VTI) media to derive more stable FD and hybrid FD/FFD migrations for such media. Our analysis of the dispersion relation of the new method indicates that it should provide more stable migration results with less artifacts and higher accuracy at steep dips. These studies lead to the conclusion that the rotation angle of the branch cut that should yield the most stable image is 60°*. This result is confirmed by the numerical impulse responses and synthetic data examples.*

INTRODUCTION

Wave-equation migration algorithms have performed better than ray-based migration methods when the velocity model has strong lateral velocity variations. One drawback of one-way wave-equation migrations, though, is their general difficulty to image steep dips. However, recent advances, particularly for finite-difference (FD) (Claerbout, 1971) and Fourier finite-difference (FFD) migrations (Ristow and Rühl, 1994) can provide wide-angle approximations for the one-way continuation operators, thus improving the imaging of steep-dip reflectors.

However, standard real-valued FD and FFD migrations cannot handle evanescent waves correctly (Millinazzo et al., 1997). As a consequence, FFD algorithms tend to become numerically unstable in the presence of strong velocity variations (Biondi, 2002). To overcome this limitation, Biondi (2002) proposes an unconditionally stable extension for the FFD algorithm. Earlier, Millinazzo et al. (1997) proposed a different approach to treating these evanescent modes in ocean acoustic applications, introducing an extension of the Padé approximation called complex Padé. It consists of a rotation of the branch cut of the square-root operator from the negative axis into the complex plane. The complex Padé expansion has been used in applied geophysics. Zhang et al. (2003) use the method in finite-difference migration. However, their implementation is not optimized for wide angles. Zhang et al. (2004) propose an FFD migration based on a different realization of complex Padé. Recently, Amazonas et al. (2007) derived FD and FFD algorithms using the complex Padé approximation for isotropic media to handle evanescent waves. They demonstrated that this procedure stabilizes FD and FFD migration without requiring special treatment for the migration domain boundaries and enables an accurate migration up to higher dips.

All these methods are based on approximations to the acoustic wave equation. However, the acoustic wave equation can only be generalized to include elliptic anisotropy. More complex anisotropic phenomena cannot be described by a physically meaningful scalar wave equation. Thus, Alkhalifah (1998) used the dispersion relation for vertical transversely isotropic (VTI) elastic media to derive an approximate acoustic wave equation for P-waves in VTI media. Based on his work, several authors have developed anisotropic

FD and FFD migration methods (Ristow, 1999; Han and Wu, 2005; Nolte, 2005; Zhang et al., 2005). Generally, FD migrations are cheaper but suffer from a pseudo S-wave artifact. To overcome this problem, Fei and Liner (2008) proposed a hybrid FFD and FD algorithm for VTI media. In this paper, we combine the ideas of these authors with the complex Padé approximation to derive a more stable FD algorithm for VTI media.

METHOD

According to Alkhalifah (2000), the acoustic wave equation for VTI media is given by

$$\frac{\partial^2 P}{\partial t^2} = (1+2\eta)v_n^2\frac{\partial^2 P}{\partial x^2} + v_{p0}^2\frac{\partial^2 P}{\partial z^2} - 2\eta v_n^2 v_{p0}^2\frac{\partial^4 F}{\partial x^2 \partial z^2}, \tag{1}$$

where P is the VTI-acoustic wavefield, v_{p0} is the vertical P-wave velocity of the medium, and v_n is the NMO velocity, given by

$$v_n = v_{p0}\sqrt{1+2\delta}. \tag{2}$$

Moreover, the anellipticity parameter η is given by

$$\eta = \frac{\epsilon - \delta}{1+2\delta}, \tag{3}$$

where ϵ and δ are Thomsen's parameters (Thomsen, 1986). Alkhalifah and Tsvankin (1995) demonstrated that a representation in terms of just two anisotropic parameters, v_n and η, is sufficient to represent time-related processing. Finally, F is the second integral in time of P, i.e.,

$$F(x,z,t) = \int_0^t \int_0^{t'} P(x,z,\tau)d\tau\, dt'. \tag{4}$$

Applying the Fourier transform in x, z and t to equation (1) leads to the following dispersion relation

$$k_z^2 = \frac{v_n^2}{v_{p0}^2}\left(\frac{\omega^2}{v_n^2} - \frac{\omega^2\, k_x^2}{\omega^2 - 2\eta v_n^2\, k_x^2}\right), \tag{5}$$

where k_x is the horizontal wavenumber and ω is the angular frequency,

From Fei and Liner (2008), we use the following notation

$$u^2 = \frac{k_x^2\, v_n^2}{\omega^2}. \tag{6}$$

Taking the square root of equation (5) using equation (6) yields

$$k_z = \frac{\omega}{v_{p0}}\sqrt{1 - \frac{u^2}{1-2\eta\, u^2}}, \tag{7}$$

where the sign for downward propagation has been chosen. For $\eta = 0$, equation (7) reduces to the elliptically anisotropic one, which differs from the isotropic one only by a constant scale factor v_n/v_{p0}. Note that the anisotropic denominator is smaller than one, which makes anisotropic migration generally more unstable than isotropic migration.

In analogy to the small dip-angle approximation of the corresponding isotropic expression (Ristow and Rühl, 1994), the square root in equation (7) can also be expanded into a Taylor series at point $u = 0$ (Fei and Liner, 2008). This leads to

$$\sqrt{1 - \frac{u^2}{1-2\eta\, u^2}} \approx 1 - \frac{1}{2}u^2 - \frac{g_2}{8}u^4 - \frac{g_3}{16}u^6, \tag{8}$$

where

$$g_2 = 1 + 8\eta, \tag{9}$$

$$g_3 = 1 + 8\eta + 32\eta^2. \tag{10}$$

Note that setting $\eta = 0$, i.e., $g_1 = g_2 = 1$ in equation (8) recovers the approximation of Ristow and Rühl (1994), which is valid for isotropic or elliptically anisotropic media.

Complex Padé FD approximation

In this section, we derive the complex Padé approximation for the above dispersion relation, because we want a steep-dip approximation and improved stability by better handling of evanescent waves. For this purpose, we have to represent the square-root in equation (7) using the complex Padé expansion.

Real Padé approximation A formal representation for square-root operator is based on the Padé expansion (Bamberger et al., 1988):

$$\sqrt{1-X^2} \approx 1 - \sum_{n=1}^{N} \frac{a_n X^2}{1 - b_n X^2}, \tag{11}$$

where for our anisotropic k_z of equation (7),

$$X^2 = \frac{u^2}{1 - 2\eta\, u^2}. \tag{12}$$

The number of terms N of the expansion should, in principle, be infinite, but in practice, generally two to four terms suffice for a reasonable approximation. The coefficients a_n and b_n are (Bamberger et al., 1988):

$$a_n = \frac{2}{2N+1} \sin^2 \frac{n\,\pi}{2N+1}, \tag{13}$$

$$b_n = \cos^2 \frac{n\,\pi}{2N+1}. \tag{14}$$

Equation (11) is known to provide an acceptable approximation up to a certain limiting dip angle. The range of dip angles can be extended by using more terms in the series. However, if $X^2 > 1$ in equation (11), the left side is a purely imaginary number, while the right side remains a real-valued quantity. In other words, the approximation breaks down. Physically, this means that approximation (11) cannot properly handle evanescent modes. This causes numerical instabilities and is responsible for the unstable behavior of the FFD algorithm in the presence of strong velocity variations (Biondi, 2002).

Complex Padé approximation To overcome these limitations, Millinazzo et al. (1997) proposed a complex representation of the Padé expansion in equation (11). They achieve this goal by rotating the branch cut of the square root into the complex plane. Their final expression is

$$\sqrt{1-X^2} \approx C_0 - \sum_{n=1}^{N} \frac{A_n X^2}{1 - B_n X^2}, \tag{15}$$

where

$$A_n = \frac{a_n e^{-i\alpha/2}}{[1 + b_n(e^{-i\alpha} - 1)]^2}, \tag{16}$$

$$B_n = \frac{b_n e^{-i\alpha}}{1 + b_n(e^{-i\alpha} - 1)}, \tag{17}$$

$$C_0 = e^{i\alpha/2} \left[1 + \sum_{n=1}^{N} \frac{a_n(e^{-i\alpha} - 1)}{1 + b_n(e^{-i\alpha} - 1)} \right], \tag{18}$$

where α is the rotation angle of the branch cut of the square root in the complex plane. The values A_n and B_n are the complex Padé coefficients, with a_n and b_n being the real ones as defined in equations (13) and (14), respectively.

Thus, expanding k_z of equation (7) into a complex Padé series, we find

$$k_z = \frac{\omega}{v_{p0}} \left[C_0 - \sum_{n=1}^{N} \frac{A_n X^2}{1 - B_n X^2} \right] \tag{19}$$

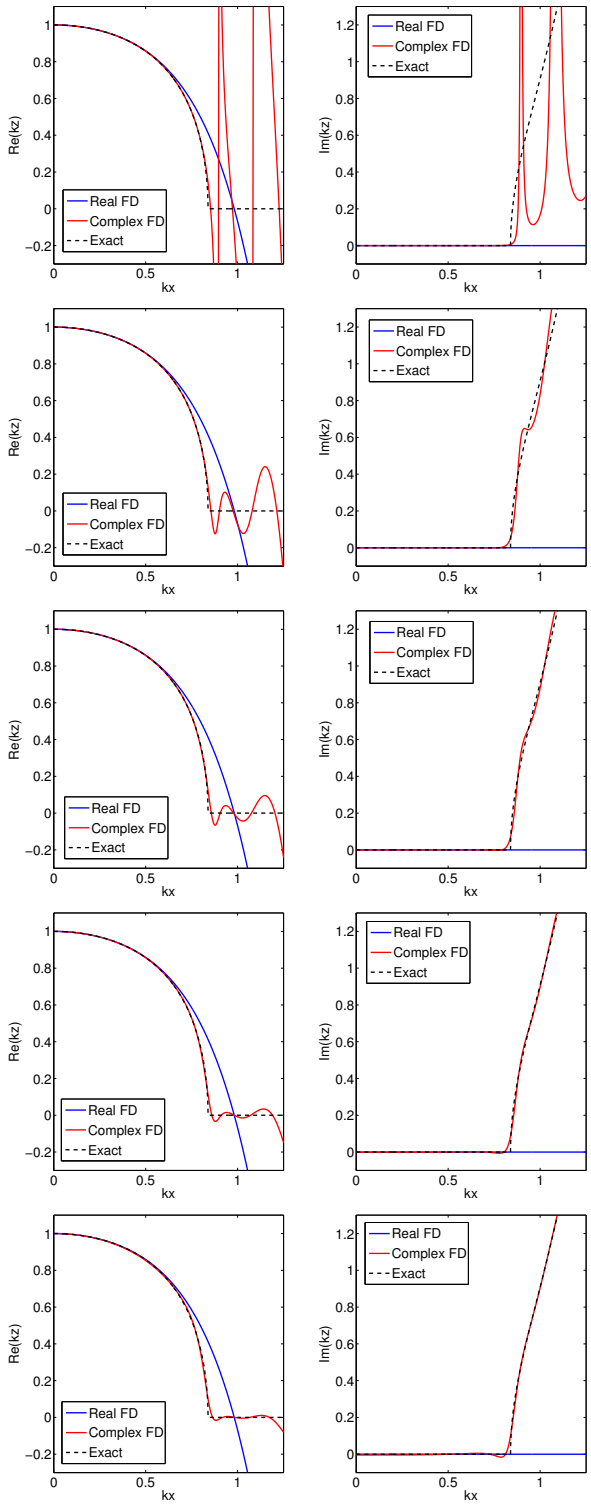

Figure 1: Complex Padé FD approximation for the dispersion relation of the one-way wave equation, computed with three terms and different rotation angles. First: $\alpha = 5°$, Second: $\alpha = 45°$, Third: $\alpha = 60°$, Forth: $\alpha = 75°$, Fifth $\alpha = 90°$. Left: Real part. Right: Imaginary part.

with X defined in equation (12). This is the *2D anisotropic complex-Padé finite-difference depth migration operator in VTI media*. Note that, as before, setting $\eta = 0$ in equation (12) leads to the corresponding operator for isotropic and elliptically anisotropic media.

To evaluate the quality of the complex Padé FD approximation (19), Figure 1 shows its comparison with the exact dispersion relation and its real Padé approximation for a homogeneous medium with $\epsilon = 0.21$ and $\delta = -0.032$, i.e., $\eta = 0.17$. Corresponding tests with different values of η exhibit a similar behavior. The FD approximation was calculated using three terms of the Padé series with five different rotation angles of $\alpha = 5^\circ$, $\alpha = 45^\circ$, $\alpha = 60^\circ$, $\alpha = 75^\circ$, and $\alpha = 90^\circ$. The improvement in the approximation of the real part of the dispersion relation with increasing α is evident. The blessings are a bit more mixed for the imaginary part. While the approximation in the evanescent region improves for increasing α, there is a short interval of negative imaginary part immediately before the evanescent region, which increases with α. Note that this negative imaginary part will cause the corresponding waves to increase exponentially, thus causing instabilities.

For this reason, the best Padé FD approximation of the imaginary part is actually achieved for a rotation angle of about 60°, where the approximation of the real part is already quite good while there is still no zone of negative imaginary part. Since the main numerical instabilities of an FD migration are caused by incorrectly treated evanescent waves, it is to be expected that a rotation angle of about 60° will produce the cleanest migrated image with the least artifacts. Note, however, that even a rotation by a small angle improves the behavior of the FD approximation (see top part of Figure 1). Although it creates rather strong fluctuation in the evanescent domain of the real part of k_z, it already introduces a nonzero imaginary part, meaning that the incorrect evanescent modes at least will be attenuated. In this respect, it is important to note that the peaks in the imaginary part, representing the strongest damping, coincide with peaks in the real part that indicate the most incorrect propagation behavior.

Complex Padé FFD approximation

Using the complex the Padé expansion, we can also derive a corresponding *2D anisotropic complex-Padé Fourier finite-difference depth migration operator in VTI media* (see Appendix A). It is given by

$$k_z = \frac{\omega}{c}\left\{\sqrt{1-\frac{c^2}{v_n^2}u^2} + C_0(p_0-1) - \sum_{n=1}^{N} A_n\, u^2 \left(\frac{p_0 - p_n^2}{1-(B_n + 2\eta + B_n\, p_n^2)\, u^2}\right)\right\}, \qquad (20)$$

where c is the constant velocity of the isotropic reference medium, and where $p_0 = c/v_{p0}$ and $p_n = c/v_n$. Note that, equation (20) has a phase-shift part, a split-step part and a finite-difference part, like in the case of the real Padé approximation (Ristow and Rühl, 1994). Our implementation of the third part of equation (20) uses a Crank-Nicholson FD scheme.

To evaluate the quality of the complex Padé FFD approximation (20), Figure 2 shows its comparison with the exact dispersion relation and its real FFD approximation for a homogeneous medium with $p_0 = 0.5$, $\epsilon = 0.21$ and $\delta = -0.032$. The FFD approximation was calculated using terms of the series with five different rotation angles of $\alpha = 5^\circ$, $\alpha = 45^\circ$, $\alpha = 60^\circ$, $\alpha = 75^\circ$, and $\alpha = 90^\circ$. We immediately recognize the improvement in the approximation of the real part of the dispersion relation in comparison to the real Padé approximation. Its dependence on α, however, is negligible. On the other hand, the approximation of the imaginary part in the evanescent region improves for increasing α. While the approximation does not recover the imaginary part correctly, the damping of the evanescent waves increases with α, thus stabilizing the migration process.

For this reason, the best Padé FFD approximation of the imaginary part is actually achieved for a rotation angle of 90°. Note, however, that even a rotation of 45° improves the behavior of the FFD approximation (see Figure 2).

Hybrid FFD/FD migration

It is important to recognize that the acoustic VTI wave equation (1) has two solutions (Alkhalifah, 2000). One of these solutions is the desired result representing a wavefront coincident with the elastic compressional wavefront. The other solution is an additional event, which has previously been observed in full

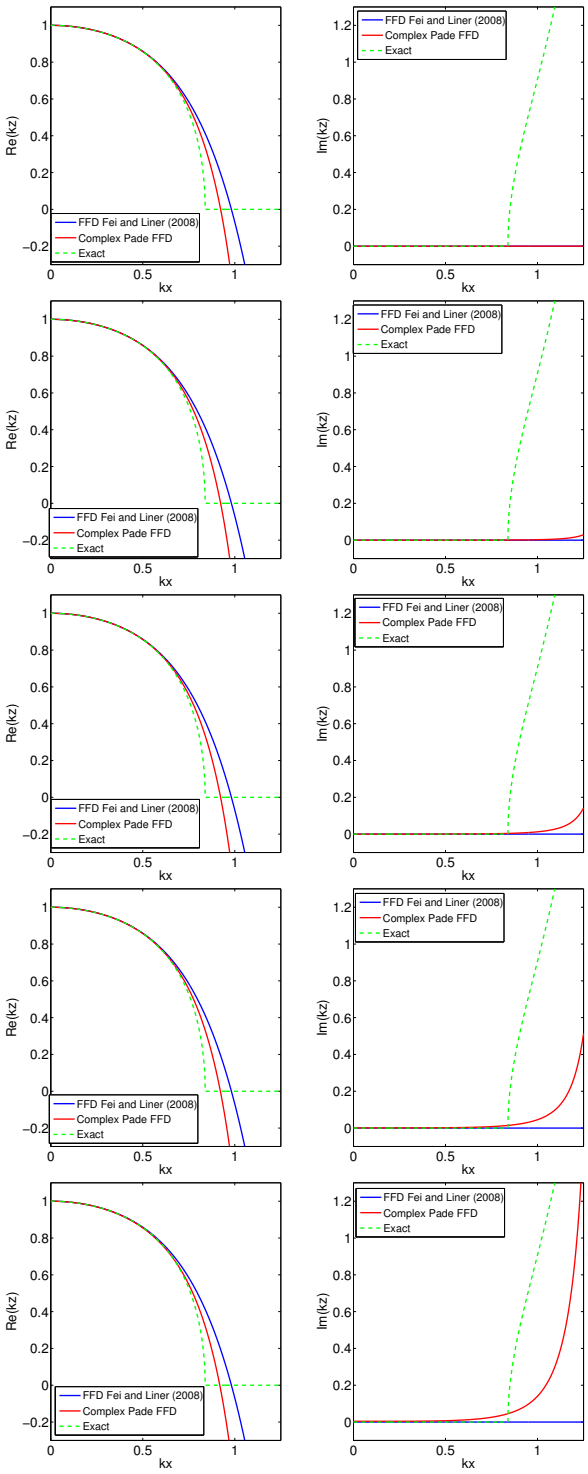

Figure 2: Complex Padé FFD approximation for the dispersion relation of the one-way wave equation, computed with three terms and different rotation angles. First: $\alpha = 5°$, Second: $\alpha = 45°$, Third: $\alpha = 60°$, Forth: $\alpha = 75°$, Fifth $\alpha = 90°$. Left: Real part. Right: Imaginary part.

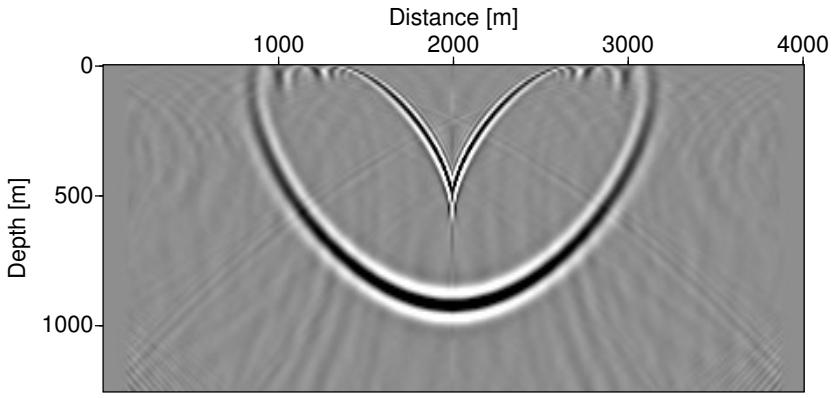

Figure 3: Real Padé ($\alpha = 0°$) FD migration for an impulse response for a constant-velocity VTI medium. The anisotropy parameters are $v_{p0} = 2800\ m/s$, $\epsilon = 0.21$ and $\delta = -0.032$.

waveform modeling. However, apparently this additional event was not always understood as a second solution to the acoustic VTI wave equation. Therefore, it has been labeled as numerical artifact (Grechka et al., 2004), sometimes called the pseudo-S-wave artifact Fei and Liner (2008). Alkhalifah (2000) solved equation (1) analytically and observed that the undesired solution can be eliminated with proper initial conditions. However, such initial conditions would have to be medium dependent and are thus very hard to find.

Since the FD algorithm calculates a numerical solution of the above acoustic VTI wave equation, it will generally find a superposition of both theoretical solutions. Tests by Alkhalifah (2000) indicate that the second solution does not develop if the source is located in an isotropic region. Thus, he suggests to place the source in an isotropic layer to suppress it.

Instead, Fei and Liner (2008) seek a more general algorithm that does not include the additional solution, so that the source can be placed arbitrarily in an anisotropic medium. They demonstrated that the event can be eliminated by a hybrid application of FFD and FD migrations. Since we already have studied the complex Padé approximation for both FD and FFD migration, it is only natural to use the idea developed by Fei and Liner (2008) to propose a complex-Padé hybrid FD/FFD depth migration.

NUMERICAL EXAMPLES

As a next step, we investigate the numerical behavior of the proposed complex-Padé VTI FD and FFD migration methods.

Impulse Response Test

First, we investigate the impulse response of the acoustic VTI wave equation (1). As a reference, Figure 3 shows the impulse response at $t = 0.5$ s of a real Padé ($\alpha = 0°$) FD migration for a homogeneous (constant velocity, constant η) VTI medium. The source pulse is a Ricker pulse with peak frequency of 25 Hz. The migration was carried out using three terms in the Padé expansion. The most prominent features in Figure 3 are the two strong events that are the two solutions of the acoustic VTI wave equation, i.e., the desired qP wavefront and the undesired pseudo-S wave (V-shaped second arrival). Additionally, we immediately note some background noise resulting from instabilities. These instabilities appear everywhere in the Figure, even causing noncausal events. They are the largest at near horizontal propagation where the influence of incorrectly treated evanescent waves is the strongest.

Figure 4 depicts the same impulse response of the corresponding complex Padé FD migration in the same medium, using a rotation angle of $\alpha = 05°$, $\alpha = 45°$, $\alpha = 60°$, $\alpha = 75°$ and $\alpha = 90°$, respectively. While the complex Padé approximation cannot eliminate the pseudo S-wave, it greatly reduces the instabilities in all panels of Figure 4. Note in particular that even the rotation angle of $5°$ almost eliminates most of the noncausal events in spite of its rather poor approximation of the evanescent part of the dispersion

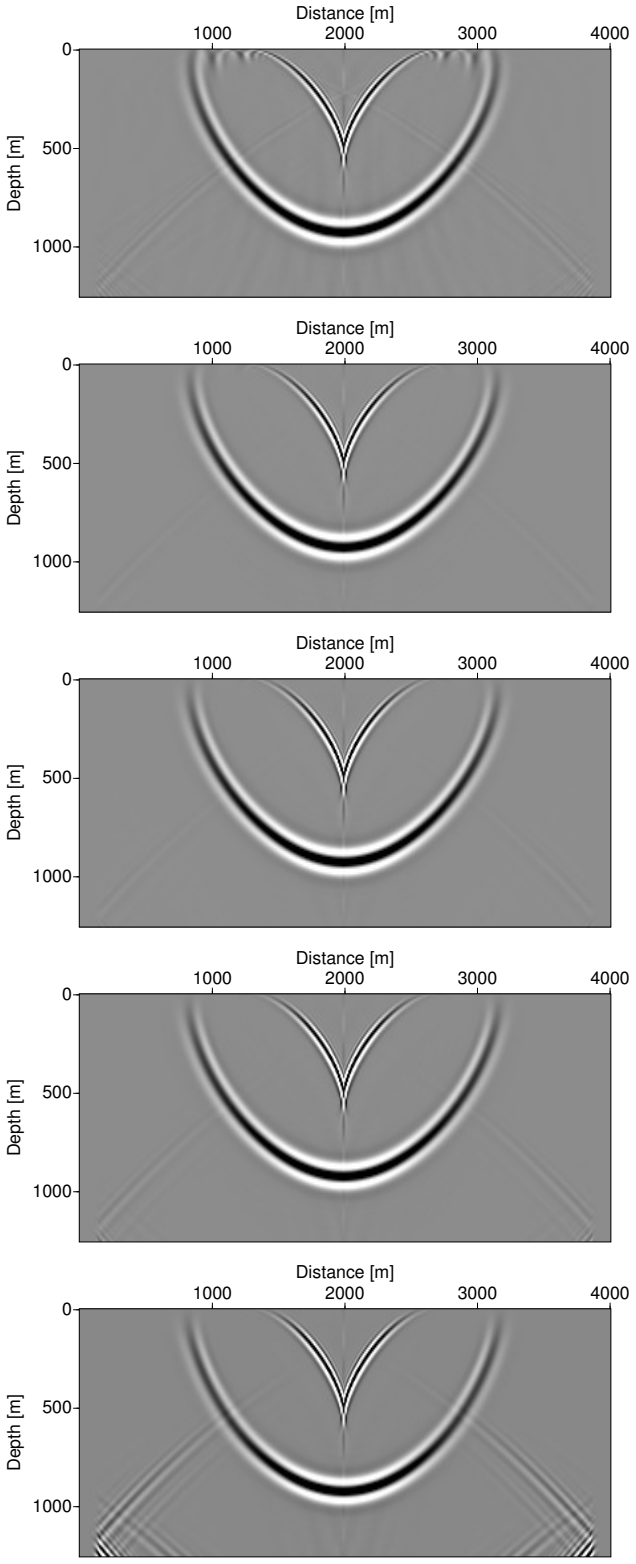

Figure 4: Complex Padé FD migration for an impulse response for a constant-velocity VTI medium. The anisotropy parameters are $v_{p0} = 2800\ m/s$, $\epsilon = 0.21$ and $\delta = -0.032$. First: $\alpha = 5°$, Second: $\alpha = 45°$, Third: $\alpha = 60°$, Forth: $\alpha = 75°$, Fifth $\alpha = 90°$.

relation.

As a final, more subtle difference between Figures 3 and 4, we note that while all impulse responses have energy up to high propagation angles, the real Padé approximation produces a slightly stronger distortion of the shape of the desired event at steep dips, causing it to bend inwards at the top. The improvement achieved by the complex Padé representation is a consequence of the better approximation of the dispersion relation in the high-angle range.

Comparing the complex Padé FD impulse responses of Figure 4 to each other, we observe that the image for $\alpha = 60^\circ$ is the best one. At $\alpha = 5^\circ$, we still see the near horizontal artifacts of the evanescent waves. The impulse responses for $\alpha = 45^\circ$ and $\alpha = 60^\circ$ are equally clean. Their main difference lies in the slightly stronger inward bending of the vertical part of the impulse response at $\alpha = 45^\circ$. At higher rotation angles, the noncausal artifacts become stronger again. This is in agreement with the previous study of the dispersion relations, which also indicated that $\alpha = 60^\circ$ should be the best rotation angle for complex Padé FD migration.

Figure 5 depicts the same impulse response of the corresponding complex Padé FFD migration in the same medium, using a rotation angle of $\alpha = 05^\circ$, $\alpha = 45^\circ$, $\alpha = 60^\circ$, $\alpha = 75^\circ$ and $\alpha = 90^\circ$, respectively. Note that in these figures, the pseudo-S-wave artifacts do not appear. On the other hand, this method does not provide a good aperture of the impulse-response, i.e., steep dips are strongly reduced. Moreover, the real or complex FFD algorithm is more expensive than its corresponding FD counterpart.

Because of these drawbacks of FFD migration, Fei and Liner (2008) proposed a hybrid algorithm. This algorithm is a combination of the FD and FFD algorithms. As its real counterpart, our complex-Padé FD/FFD hybrid migration algorithm uses an FFD implementation for a few steps in z, for example 5 steps, and then carries over to the FD implementation. This algorithm is greatly advantageous, because the computation cost and accuracy is almost the same as that of the FD algorithm and it does not generate the pseudo-S-wave artifact. Figure 6 shows the impulse response of the hybrid complex-Padé migration. This figure is much cleaner the the FFD one, has more more pronounced steep dips, and a strongly reduced pseudo S-wave. To generate the impulse response of Figure 6, we used the underlying complex-Padé approximation with the optimum rotation angles, i.e., the FFD algorithm with $\alpha = 90^\circ$ and the FD algorithm with $\alpha = 60^\circ$.

Synthetic data test

We tested the complex-Padé migration algorithms on a synthetic data set courtesy of HESS. Figure 7 shows the vertical P-wave model and the distribution of Thomsen's (1986) parameters ϵ and δ. All images were constructed using a cross-correlation imaging condition.

Figure 8 shows the anisotropic (top) and isotropic (bottom) migrated sections with optimal rotation angle of $\alpha = 60^\circ$. There are some spurious events because no multiple suppression was applied. The primary reflection events appear clearly. As expected, the anisotropic migration is much better than the isotropic one.

Anisotropic complex-Padé FD migration correctly positions all reflectors, even below the salt. Isotropic complex-Padé FD migration does not completely focus the reflectors and has some with steeply dipping events. Overall, the amplitude is weaker than that of anisotropic migration.

Figure 9 shows the anisotropic complex-Padé hybrid depth migration. Actually, the images of anisotropic complex-Padé FD depth migration and anisotropic complex-Padé hybrid depth migration look practically identical. The reason is that the HESS synthetic data set has its sources in an isotropic water layer, so that the pseudo-S-wave artifact is not generated by the FD algorithm.

For this model with strong lateral velocity variations, real FD migration is unstable. Therefore, we cannot compare the complex-Padé FD algorithm with its real counterpart. To indicate the problems, Figure 10 shows the the anisotropic (top) and isotropic (bottom) migrated sections using FD algorithm with a small rotation angle of $\alpha = 5^\circ$. The anisotropic migration (top) is still suffering from instabilities due to incorrect treatment of the evanescent waves. The isotropic algorithm is somewhat more stable, so that a small rotation of the branch cut is already sufficient to completely eliminate the instabilities.

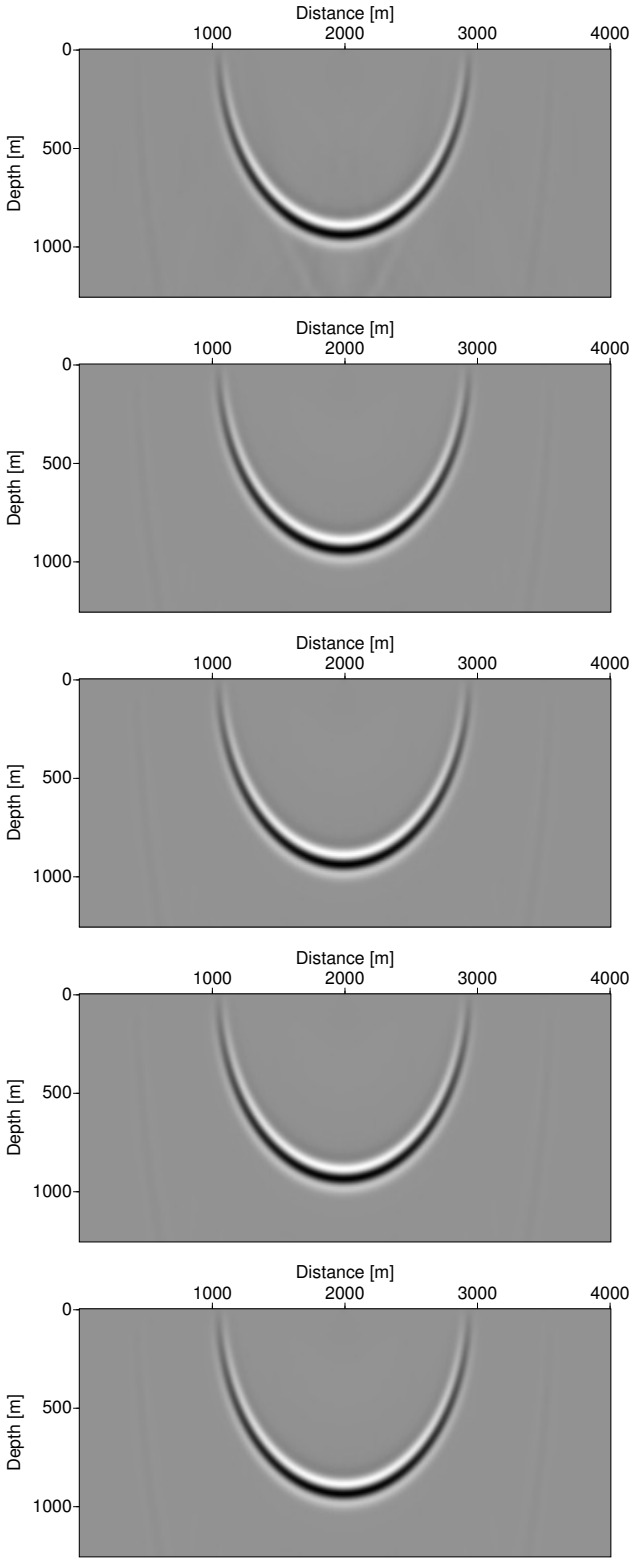

Figure 5: Complex Padé FFD migration for an impulse response for a constant-velocity VTI medium. The anisotropy parameters are $v_{p0} = 2800\ m/s$, $\epsilon = 0.21$ and $\delta = -0.032$. First: $\alpha = 5°$, Second: $\alpha = 45°$, Third: $\alpha = 60°$, Forth: $\alpha = 75°$, Fifth $\alpha = 90°$.

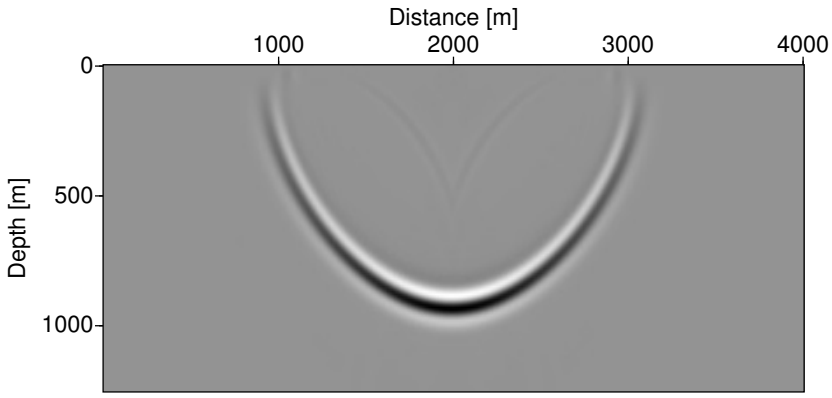

Figure 6: Hybrid complex-Padé migration for an impulse response for a constant-velocity VTI medium. The anisotropy parameters are $v_{p0} = 2800\ m/s$, $\epsilon = 0.21$ and $\delta = -0.032$. For the hybrid migration, we used the optimum rotation angle for each individual algorithm, i.e., $\alpha = 90^\circ$ for the FFD part and $\alpha = 60^\circ$ for the FD part.

CONCLUSIONS

In this work, we have combined the anisotropic migration for VTI media using the acoustic VTI wave equation of Alkhalifah (2000) with the complex Padé FD approximation of Amazonas et al. (2007) to derive a more stable VTI migration method. Our studies of the dispersion relation of the new method indicate that it should provide more stable migration results with less artifacts and higher accuracy at steep dips. The best rotation angle of the branch cut turns out to be 60°. This result is confirmed by the numerical impulse responses. A synthetic data example demonstrates the improved stability and reduced artifacts of complex Padé FD and FD/FFD hybrid migrations.

ACKNOWLEDGMENTS

We thank Hess Corporation for the synthetic data. This work was kindly supported by the Brazilian research agencies CNPq and FAPESP (proc. 06/04410-5), as well as Petrobras and the sponsors of the *Wave Inversion Technology (WIT) Consortium*.

REFERENCES

Alkhalifah, T. (1998). Acoustic approximations for processing in transversely isotropic media. *Geophysics*, 63(2):623–631.

Alkhalifah, T. (2000). An acoustic wave equation for anisotropic media. *Geophysics*, 65(4):1239–1250.

Alkhalifah, T. and Tsvankin, I. (1995). Velocity analysis for transversely isotropic media. *Geophysics*, 60(5):1550–1566.

Amazonas, D., Costa, J. C., Schleicher, J., and Pestana, R. (2007). Wide-angle FD and FFD migration using complex Padé approximations. *Geophysics*, 72(6):S215–S220.

Bamberger, A., Engquist, B., Halpern, L., and Joly, P. (1988). Higher order paraxial wave equation approximations in heterogeneous media. *J. Appl. Math.*, 48:129–154.

Biondi, B. (2002). Stable wide-angle Fourier finite-difference downward extrapolation of 3-D wavefields. *Geophysics*, 67(3):872–882.

Claerbout, J. F. (1971). Toward a unified theory of reflector mapping. *Geophysics*, 36(3):467–481.

Fei, T. W. and Liner, C. L. (2008). Hybrid Fourier finite-difference 3D depth migration for anisotropic media. *Geophysics*, 73(2):S27–S34.

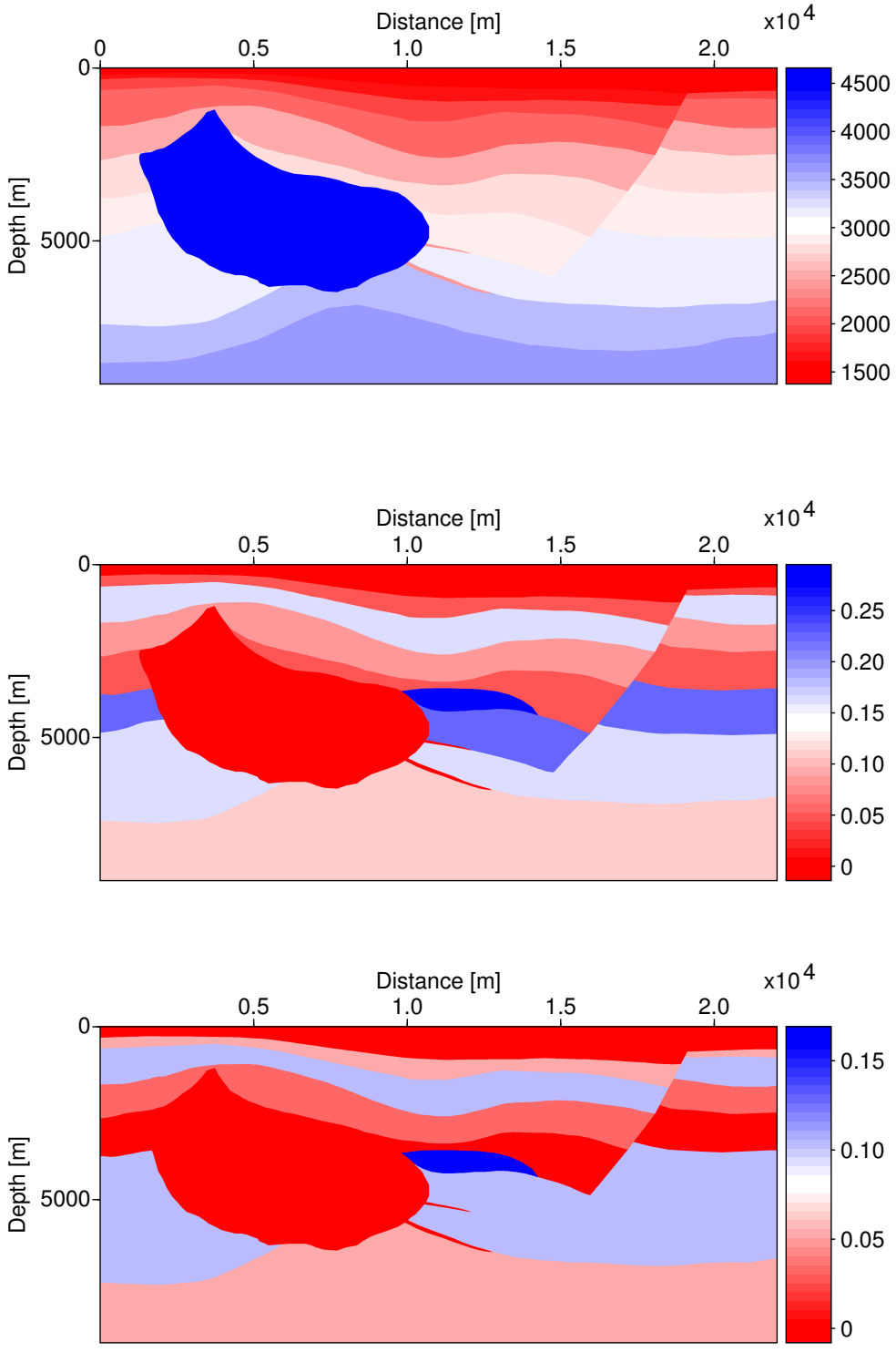

Figure 7: Synthetic model (courtesy of HESS). Top: vertical velocity; center: ϵ; bottom: δ.

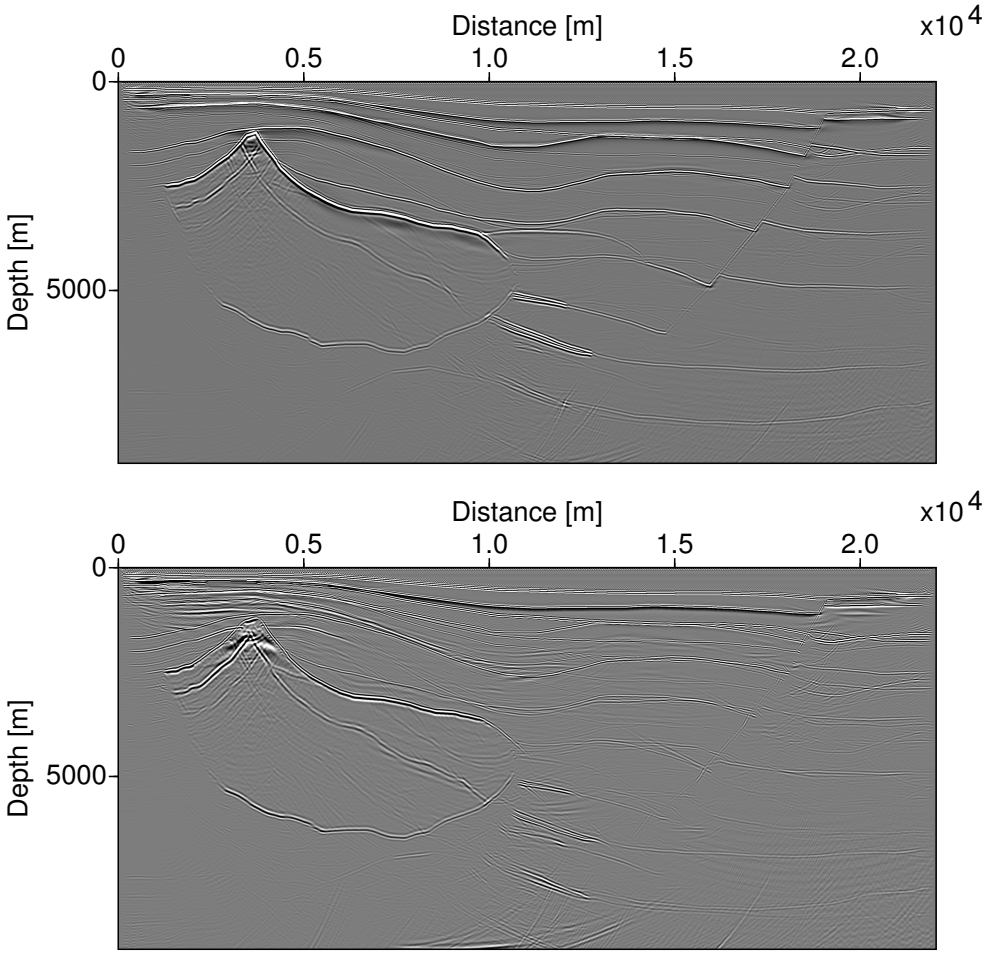

Figure 8: Migrated sections using complex-Padé FD depth migration. Top: Anisotropic algorithm, Bottom: Isotropic algorithm.

Grechka, V., Zhang, L., and Rector III, J. W. (2004). Shear waves in acoustic anisotropic media. *Geophysics*, 69(2):576–582.

Han, Q. and Wu, R.-S. (2005). A one-way dual-domain propagator for scalar qP-waves in VTI media. *Geophysics*, 70(2):D9–D17.

Millinazzo, F. A., Zala, C. A., and Brooke, G. H. (1997). Square-root approximations for parabolic equation algorithms. *J. Acoust. Soc. Am.*, 101(2):760–766.

Nolte, B. (2005). Converted-wave migration for VTI media using Fourier finite-difference depth extrapolation. *EAGE, Expanded Abstracts*, page P001.

Ristow, D. (1999). Migrations in transversely isotropic media using implicit finite-difference operators. *Journal of Seismic Exploration*, 8(1):39–55.

Ristow, D. and Rühl, T. (1994). Fourier finite-difference migration. *Geophysics*, 59(12):1882–1893.

Thomsen, L. (1986). Weak elastic anisotropy. *Geophysics*, 51(10):1954–1966.

Zhang, L., Hua, B., and Calandra, H. (2005). 3D Fourier finite difference anisotropic depth migration. *SEG Technical Program Expanded Abstracts*, 24(1):1914–1917.

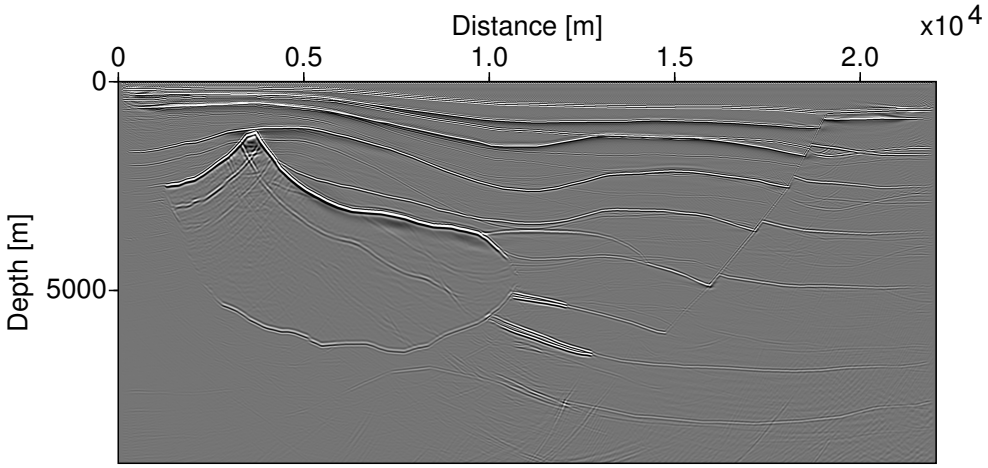

Figure 9: Migrated section using complex-Padé hybrid depth migration.

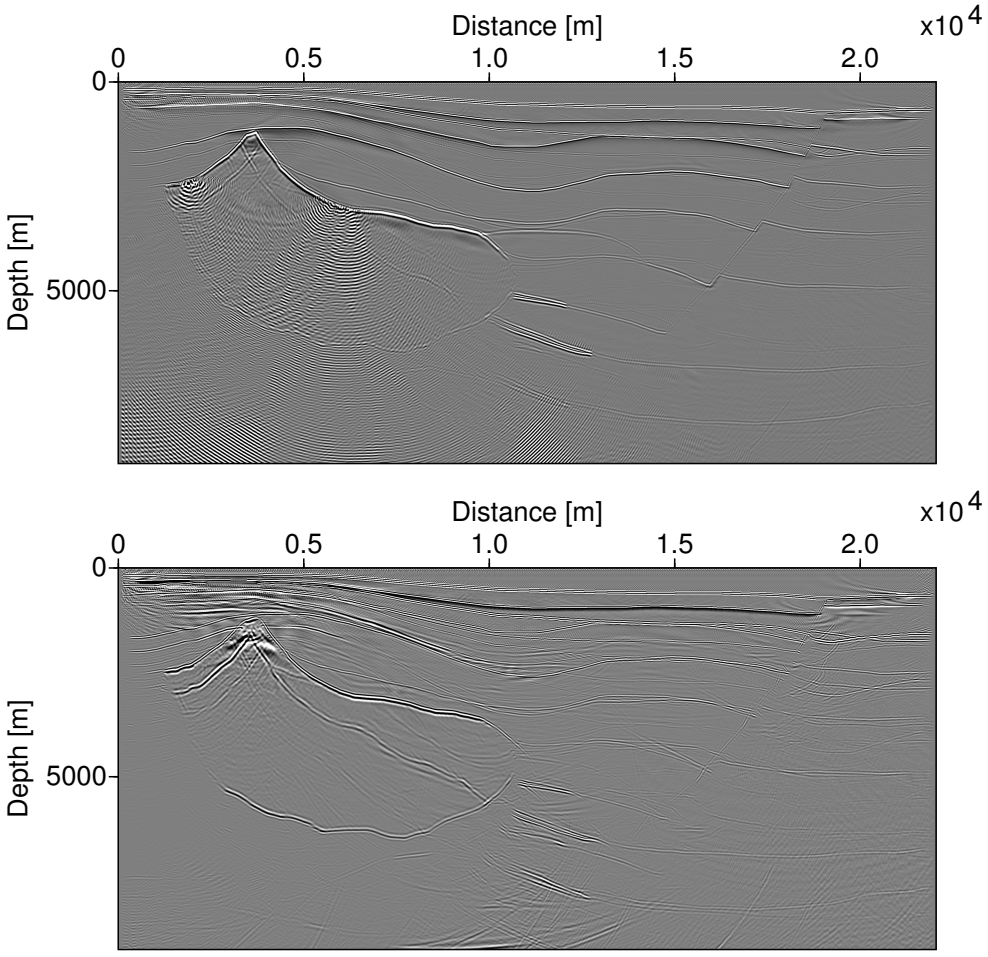

Figure 10: Migrated sections using complex-Padé FD depth migration with $\alpha = 5^{\circ}$. Top: Anisotropic algorithm, Bottom: Isotropic algorithm.

Zhang, L., Rector, J. W., and Hoversten, G. M. (2003). Split-step complex Padé migration. *Journal of Seismic Exploration*, 12:229–236.

Zhang, L., Rector, J. W., Hoversten, G. M., and Fomel, S. (2004). Split-step complex Padé-Fourier depth migration. *SEG Int'l Exposition and 74th Annual Meeting*.

APPENDIX A

.1 FFD DISPERSION RELATION

In this appendix we derive the FFD dispersion relation for VTI media. Starting from equation (7), we can write

$$k_z = \frac{\omega}{c}\sqrt{1-\frac{c^2}{v_n^2}u^2}+\frac{\omega}{c}\left[\frac{c}{v_{p0}}\sqrt{1-\frac{u^2}{1-2\eta\,u^2}}-\sqrt{1-\frac{c^2}{v_n^2}u^2}\right], \tag{21}$$

where c is the constant velocity of the isotropic reference medium. Introducing the notations $p_0 = c/v_{p0}$ and $p_n = c/v_n$, this can be recast into the form

$$k_z = \frac{\omega}{c}\sqrt{1-\frac{c^2}{v_n^2}u^2}+\frac{\omega}{c}\left[p_0\sqrt{1-\frac{u^2}{1-2\eta\,u^2}}-\sqrt{1-p_n^2\,u^2}\right] \tag{22}$$

$$\approx \frac{\omega}{c}\left\{\sqrt{1-\frac{c^2}{v_n^2}u^2}+p_0\left[C_0-\sum_{n=1}^{N}\frac{A_n\,X^2}{1-B_n\,X^2}\right]-\left[C_0-\sum_{n=1}^{N}\frac{A_n\,p_n^2\,u^2}{1-B_n\,p_n^2\,u^2}\right]\right\} \tag{23}$$

$$\approx \frac{\omega}{c}\left\{\sqrt{1-\frac{c^2}{v_n^2}u^2}+C_0(p_0-1)-\sum_{n=1}^{N}\left(\frac{A_n\,p_0\,X^2}{1-B_n\,X^2}-\frac{A_n\,p_n^2\,u^2}{1-B_n\,p_n^2\,u^2}\right)\right\} \tag{24}$$

$$\approx \frac{\omega}{c}\left\{\sqrt{1-\frac{c^2}{v_n^2}u^2}+C_0(p_0-1)-\sum_{n=1}^{N}A_n\,u^2\left(\frac{p_0}{1-(B_n+2\eta)\,u^2}-\frac{p_n^2}{1-B_n\,p_n^2\,u^2}\right)\right\} \tag{25}$$

$$\approx \frac{\omega}{c}\left\{\sqrt{1-\frac{c^2}{v_n^2}u^2}+C_0(p_0-1)-\sum_{n=1}^{N}A_n u^2\left(\frac{p_0(1-B_np_n^2u^2)-p_n^2[1-(B_n+2\eta)u^2]}{[1-(B_n+2\eta)u^2](1-B_np_n^2u^2)}\right)\right\}. \tag{26}$$

Neglecting terms of fourth order,

$$k_z = \frac{\omega}{c}\left\{\sqrt{1-\frac{c^2}{v_n^2}u^2}+C_0(p_0-1)-\sum_{n=1}^{N}A_n\,u^2\left(\frac{p_0-p_n^2}{1-(B_n+2\eta+B_n\,p_n^2)\,u^2}\right)\right\} \tag{27}$$